








Genotoxic stress triggers the activation of IRE1 α -dependent RNA decay to modulate the DNA damage response

Estefanie Dufey^{1,2,3}, José Manuel Bravo-San Pedro^{4,5}, Cristian Eggers^{6,7}, Matías González-Quiroz ^{1,2,3,8,9}, Hery Urrea^{1,2,3}, Alfredo I. Sagredo^{1,2,3}, Denisse Sepulveda^{1,2,3}, Philippe Pihán^{1,2,3}, Amado Carreras-Sureda^{1,2,3}, Younis Hazari^{1,2,3}, Eduardo A. Sagredo¹⁰, Daniela Gutierrez¹¹, Cristian Valls¹¹, Alexandra Papaioannou ^{8,9}, Diego Acosta-Alvear^{12,13,14}, Gisela Campos¹⁵, Pedro M. Domingos ¹⁶, Rémy Pedeux^{8,9}, Eric Chevet ^{8,9}, Alejandra Alvarez¹¹, Patricio Godoy¹⁵, Peter Walter ^{12,13}, Alvaro Glavic^{6,7}, Guido Kroemer ^{4,5,17,18,19} & Claudio Hetz ^{1,2,3,20} ✉

The molecular connections between homeostatic systems that maintain both genome integrity and proteostasis are poorly understood. Here we identify the selective activation of the unfolded protein response transducer IRE1 α under genotoxic stress to modulate repair programs and sustain cell survival. DNA damage engages IRE1 α signaling in the absence of an endoplasmic reticulum (ER) stress signature, leading to the exclusive activation of regulated IRE1 α -dependent decay (RIDD) without activating its canonical output mediated by the transcription factor XBP1. IRE1 α endoribonuclease activity controls the stability of mRNAs involved in the DNA damage response, impacting DNA repair, cell cycle arrest and apoptosis. The activation of the c-Abl kinase by DNA damage triggers the oligomerization of IRE1 α to catalyze RIDD. The protective role of IRE1 α under genotoxic stress is conserved in fly and mouse. Altogether, our results uncover an important intersection between the molecular pathways that sustain genome stability and proteostasis.

¹Biomedical Neuroscience Institute (BNI), Faculty of Medicine, University of Chile, Santiago, Chile. ²Center for Geroscience, Brain Health and Metabolism (GERO), Santiago, Chile. ³Program of Cellular and Molecular Biology, Institute of Biomedical Sciences, University of Chile, Santiago, Chile. ⁴Centre de Recherche des Cordeliers, Equipe labellisée par la Ligue contre le cancer, Inserm U1138, Université de Paris, Sorbonne Université, Paris, France. ⁵Metabolomics and Cell Biology Platforms, Gustave Roussy Cancer Campus, Villejuif, France. ⁶Department of Biology, Faculty of Sciences, University of Chile, Santiago, Chile. ⁷Center for Genome Regulation, Faculty of Sciences, University of Chile, Santiago, Chile. ⁸Proteostasis & Cancer Team, INSERM U1242, University of Rennes 1, Rennes, France. ⁹Centre de Lutte contre le Cancer Eugène Marquis, Rennes, France. ¹⁰Department of Molecular Biosciences, The Wenner-Gren Institute, Stockholm University, Svante Arrheniusväg 20C, 106 91 Stockholm, Sweden. ¹¹Department of Cell & Molecular Biology, Pontificia Universidad Católica de Chile, 8331010 Santiago, Chile. ¹²Department of Biochemistry and Biophysics, University of California, San Francisco, CA, USA. ¹³Howard Hughes Medical Institute, University of California, San Francisco, San Francisco, CA, USA. ¹⁴Department of Molecular, Cellular, and Developmental Biology, University of California, Santa Barbara, Santa Barbara, CA 93106, USA. ¹⁵IfADo-Leibniz Research Centre for Working Environment and Human Factors at the Technical University Dortmund, 44139 Dortmund, Germany. ¹⁶Instituto de Tecnologia Química e Biológica, Universidade Nova de Lisboa, Av. da República, 2780-157 Oeiras, Portugal. ¹⁷Pôle de Biologie, Hôpital Européen Georges Pompidou, AP-HP, Paris, France. ¹⁸Suzhou Institute for Systems Medicine, Chinese Academy of Medical Sciences, Suzhou, China. ¹⁹Department of Women's and Children's Health, Karolinska Institute, Karolinska University Hospital, Stockholm, Sweden. ²⁰The Buck Institute for Research in Aging, Novato, CA 94945, USA. ✉email: chetz@med.uchile.cl

The integrity of the genome is constantly threatened by endogenously produced toxic metabolites, physical, and chemical insults, resulting in a variety of DNA lesions. Inefficient DNA repair translates into cellular dysfunction and death, but also into the propagation of somatic mutations and malignant transformation. To limit genome instability, cells engage the DNA damage response (DDR) and activate repair mechanisms to reverse or minimize alterations in DNA integrity¹. The DDR pathway involves the interconnection of complex signaling networks that enforce cell cycle arrest and DNA repair. The failure of this adaptive mechanism is detrimental for the cell, resulting in an irreversible cell cycle arrest (senescence) or the activation of different types of regulated death programs¹. Accordingly, perturbations in the DDR largely contribute to oncogenesis, tumor progression, and the resistance to irradiation and chemotherapy with genotoxic drugs. The accumulation of synonymous mutations, aneuploidy, as well as the activation of oncogenes, deregulate proteostasis². The endoplasmic reticulum (ER) is the main subcellular compartment involved in protein folding and quality control³, representing a central node of the proteostasis network. The unfolded protein response (UPR) is a specialized mechanism to cope with ER stress^{4,5}, that also influences most hallmarks of cancer⁶. Nevertheless, the possible involvement of the UPR in the surveillance and maintenance of genome integrity remains elusive.

Inositol requiring enzyme 1 alpha (known as ERN1, referred to as IRE1 α hereafter) controls the most evolutionary conserved UPR signaling branch, regulating ER proteostasis and cell survival through distinct functional outputs⁴. IRE1 α is a serine/threonine protein kinase and endoribonuclease that catalyzes the unconventional splicing of the mRNA encoding X-Box binding protein 1 (*Xbp1*), generating an active transcription factor that enforces adaptive programs⁷. IRE1 α also degrades a subset of mRNAs and microRNAs through a process known as regulated IRE1 α -dependent decay of RNA (RIDD), impacting various biological processes, including cell death and inflammation^{8–11}. A screen aiming to define the universe of XBP1-target genes under ER stress identified a cluster of DDR-related components¹², and suboptimal DNA repair may trigger ER stress². Together, these observations suggest a link between DNA damage and ER proteostasis. Here we investigate the possible contribution of IRE1 α to the DDR. Surprisingly, we observed that genotoxic stress engages IRE1 α signaling in the absence of ER stress markers. In fibroblasts undergoing DNA damage, IRE1 α activation results in the selective activation of RIDD in the absence of XBP1 mRNA splicing, impacting genome stability, cell survival and cell cycle control. At the molecular level, we identify specific RIDD mRNA substrates as possible effectors of the phenotypes triggered by IRE1 α deficiency. We also validated the significance of IRE1 α signaling to the DDR in vivo using genetic manipulation in mouse and fly models. Our results suggest that IRE1 α has an alternative function in cells undergoing genotoxic stress, where it serves to amplify and sustain an efficient DDR to maintain genome stability and cell survival.

Results

DNA damage selectively induces IRE1 α signaling toward RIDD. Upon ER stress, IRE1 α dimerization leads to its autophosphorylation and the formation of large clusters that are needed for optimal signaling¹³. Exposure of mouse embryonic fibroblasts (MEF) to the DNA damaging agent etoposide, a topoisomerase II inhibitor, triggers mild IRE1 α phosphorylation (Fig. 1a) and formation of IRE1 α clusters, as revealed using an IRE1 α -GFP reporter (Fig. 1b). Similar results were obtained in cells exposed to γ -irradiation (Supplementary Fig. 1a). Unexpectedly, MEF cells

stimulated with etoposide or γ -irradiation failed to engage *Xbp1* mRNA splicing, as determined by two independent PCR-based assays (Fig. 1c, d) or western blot analysis (Supplementary Fig. 1b). Moreover, no signs of ER stress were observed in cells undergoing DNA damage when we assessed canonical markers of UPR activation, including the expression of CHOP, ATF4, BiP, as well as ATF6 processing and the phosphorylation of both PERK and eIF2 α (Supplementary Fig. 1c, d). As positive controls of DNA damage, we monitored the levels of phosphorylation of the histone H2AX (γ -H2AX) or the upregulation of the cyclin-dependent kinase inhibitor CDKN1A (also known as *p21*) (Supplementary Fig. 1b, d). Unexpectedly, classical RIDD mRNA substrates such as *Bloc1s1* and *Sparc*^{8,9} decayed upon exposure to DNA damaging agents (Fig. 1e). Importantly, this decrease in *Bloc1s1* and *Sparc* mRNAs did not occur in IRE1 α -deficient cells (Fig. 1e), nor upon pharmacological inhibition of the RNase activity of IRE1 α with MKC-8866 (Supplementary Fig. 1e, f), confirming the occurrence of RIDD. These results suggest that DNA damage selectively stimulates IRE1 α activity toward RIDD and not *Xbp1* mRNA splicing in the absence of global ER stress markers.

IRE1 α regulates DDR signaling under genotoxic stress. To evaluate the significance of IRE1 α expression to the adaptive capacity of cells undergoing DNA damage, we compared the viability of IRE1 α -deficient and control (wild type, WT) cells after exposure to various agents that induce distinct types of DNA lesions, including etoposide, 5-hydroxyurea, 5-fluorouracil, and γ -irradiation. Remarkably, IRE1 α deficiency sensitized cells to all types of genotoxic stress, thus increasing the incidence of cell death (Fig. 1f and Supplementary Fig. 2a). We confirmed these results by measuring caspase-3 activation, a marker of apoptosis (Fig. 1g). We then stably reconstituted IRE1 α null cells with an HA-tagged version of IRE1 α (IRE1 α -HA) that expresses levels similar to endogenous (described in refs. 14,15). Importantly, the hypersensitivity of IRE1 α deficient cells to DNA damage was partially reverted by expressing IRE1 α -HA, suggesting that the phenotypes observed in IRE1 α -deficient cells under genotoxic stress are a primary phenotype, and are not due to clonal effects or compensatory changes (Supplementary Fig. 2b). In sharp contrast, IRE1 α knockout MEFs did not reveal any differential sensitivity to the ER stress inducer tunicamycin, in line with prior results based on pharmacological inhibition of IRE1 α ¹⁶. Also, the pharmacological inhibition of IRE1 α RNase activity with MKC-8866 increases the susceptibility to cell death after prolonged genotoxic treatments (Fig. 1h, i). These findings highlight the importance of IRE1 α in the adaptation response to DNA damage.

The downstream effects of the DDR are mediated by the activity of check point kinases CHK1 and CHK2, engaging the tumor suppressor protein P53 to induce cell-cycle arrest and the transcription of DNA damage-responsive genes, or to trigger apoptotic cell death¹⁷. DDR signaling translates into the phosphorylation of histone H2AX (γ -H2AX), and the rate of γ -H2AX decay after DNA injury is a sign of DNA repair. Thus, we monitored the kinetics of H2AX (de)phosphorylation after exposing cells to a pulse of etoposide. IRE1 α null cells exhibited a lower response and faster attenuation of γ -H2AX phosphorylation compared to cells in which IRE1 α was reintroduced (Fig. 2a). Similar results were obtained when cells where exposed to a shorter pulse of a higher concentration of etoposide (Supplementary Fig. 2c). Analysis of nuclear γ -H2AX foci by immunofluorescence and confocal microscopy also indicated reduced γ -H2AX phosphorylation in IRE1 α deficient cells (Fig. 2b). To corroborate these results, we performed the comet assay to directly visualize the DNA damage observing that IRE1 α knockout cells exposed to etoposide exhibited increased

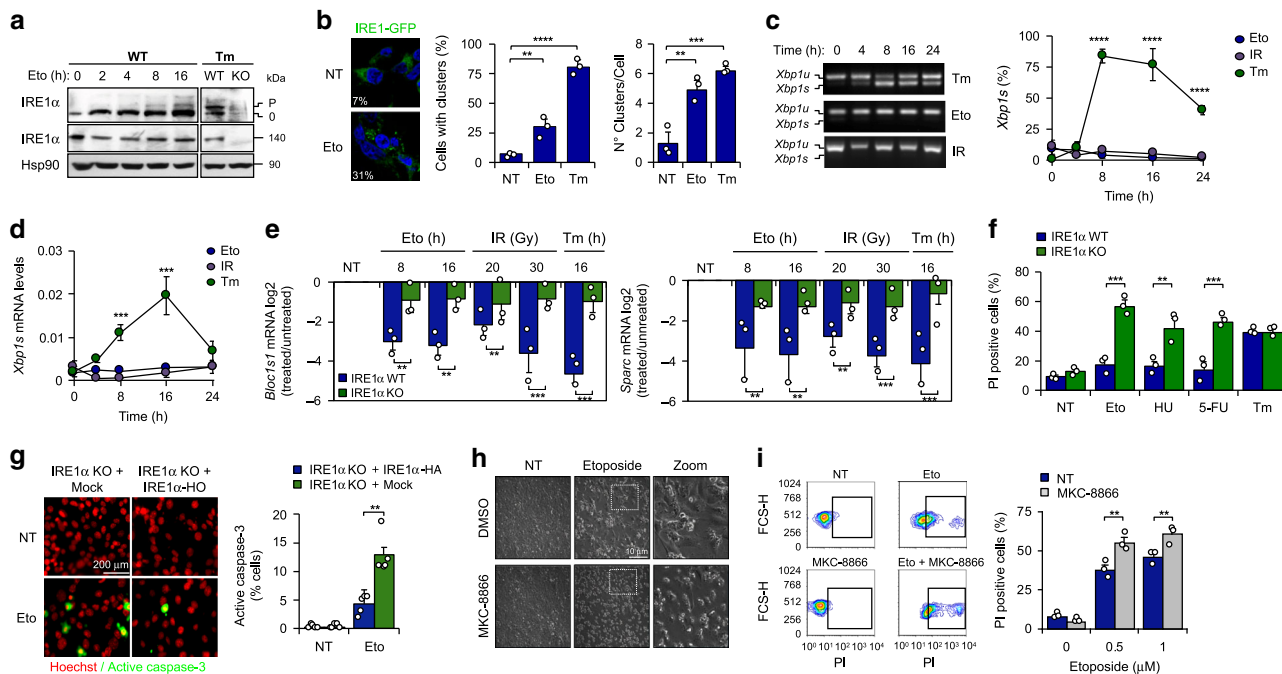


Fig. 1 Selective activation of RIDD under DNA damage. **a** MEF were treated with 10 μM etoposide (Eto) for indicated time points and phosphorylation levels of IRE1α were detected by Phostag assay (p: phosphorylated O: non-phosphorylated bands). IRE1α levels were analyzed by western blot. Treatment with 500 ng/mL tunicamycin (Tm) as positive control (8 h) (*n* = 3). **b** TREX-IRE1-3F6H-GFP cells were treated with 25 μM Eto (8 h) or 1 μg/mL Tm (4 h). IRE1-GFP foci were quantified by confocal microscopy (>200 cells, *n* = 3). **c** MEF were treated with either 100 ng/mL Tm, 10 μM Eto or 25 Gy of ionizing radiation (IR) at indicated time points. *Xbp1* mRNA splicing percentage was calculated by RT-PCR using densitometric analysis (left panel) (*n* = 3). **d** *Xbp1s* mRNA levels were quantified by real-time-PCR in samples described in **c** (*n* = 3). **e** WT and IRE1α KO cells were treated with 10 μM Eto (8 h and 16 h), IR (20 or 30 Gy, 16 h) and the decay of mRNA levels of *Bloc1s1* and *Sparc* was monitored by real-time-PCR. Treatment with 500 ng/mL Tm as positive control (*n* = 3). **f** WT and IRE1α KO cells were treated with 25 μM Eto, 1 μM 5-fluorouracil (5-FU), 1 μM hydroxyurea (HU) or 1 μg/mL Tm by 24 h and viability analyzed using propidium iodide (PI) staining and FACS (*n* = 3). **g** IRE1α KO (Mock) and IRE1α-HA reconstituted cells were treated with 10 μM Eto for 12 h and apoptosis monitored by caspase-3 positive cells (green). Nucleus (Red) was stained to visualize cells number (*n* = 3). **h** MEF cells treated 36 h with 0.5 μM Eto in combination with the IRE1α inhibitor 25 μM MKC-8866. Representative images. **i** WT cells were treated with 0.5 and 1 μM Eto or in combination with 25 μM MKC-8866 (36 h). Cell viability analyzed using PI staining and FACS (*n* = 3). All panels data is shown as mean ± s.e.m.; **p* < 0.05, ***p* < 0.01, and ****p* < 0.001, based on **b** two-tailed unpaired *t*-Student's test, (**c**, **d**). One-way ANOVA followed Tukey's test (**e-g**, **i**), two-way ANOVA followed Bonferroni's test. Data is provided as a Source Data file.

DNA damage (Fig. 2c). We also performed a cytokinesis-block micronucleus cytome (CBMN) assay as an indirect measure of DNA breaks. Cells were incubated with etoposide for 3 h, followed by the administration of cytochalasin-B (CytB) for an additional 24 h. IRE1α deficiency resulted in a higher percentage of cells with binucleated nuclei, micronuclei or nuclear buds (Fig. 2d). Altogether, these results suggest that IRE1α null cells have reduced engagement of DNA repair programs.

A direct consequence of DNA damage is cell cycle arrest. No significant differences were observed in cell proliferation (Supplementary Fig. 3a) or cell cycle progression between control and IRE1α null cells in normal conditions. Nevertheless, the fraction of cells arrested in the S and G₂/M phases was reduced in IRE1α knockout MEFs exposed to etoposide (Fig. 2e). Similar results were obtained when we reintroduced IRE1α in knockout cells (Supplementary Fig. 3b). At the molecular level, the ablation of IRE1α expression resulted in a strong attenuation in the phosphorylation of CHK1 and CHK2 in DNA-damaged cells (Fig. 2f). In contrast, the phosphorylation of the apical kinase ataxia telangiectasia mutated kinase (ATM; an upstream sensor of the DDR) was not altered in IRE1α knockout cells exposed to etoposide (Fig. 2f and Supplementary Fig. 3c). Consistent with these results, IRE1α knockout and WT MEF cells showed similar phosphorylation of SMC1¹⁸ and KAP1¹⁹, two direct substrates of ATM (Supplementary Fig. 3d), suggesting that the defects

triggered by IRE1α deficiency occur downstream of ATM activation regulating CHK1 and CHK2 activation. Moreover, IRE1α deficient cells showed a sustained kinetic of activation of P53 (Supplementary Fig. 3e). Taken together, these results suggest that IRE1α deficiency deregulates DDR signaling, thus affecting cell cycle progression, DNA repair and cell survival under genotoxic stress.

Genotoxic stress triggers RIDD to regulate DDR signaling. To obtain mechanistic insights, we attempted to identify RIDD target mRNAs that might connect IRE1α signaling to the DDR. Previously, a global in vitro screening uncovered a cluster of mRNAs containing consensus sequences cleaved by IRE1α that are associated to a stem-loop structurally similar to the *Xbp1* mRNA splicing site²⁰. Among the 13 top hits, two DDR-related genes were identified as possible RIDD substrates: PPP2CA-scaffolding A subunit (*Ppp2r1a*) and RuvB like AAA ATPase1 (*Ruvbl1*) mRNAs²¹ (Fig. 3a). PPP2R1A encodes the scaffold A subunit of protein phosphatase 2 catalytic subunit alpha (PPP2CA, also known as PP2A), which dephosphorylates check point kinases, reversing the G₂/M arrest, and directly catalyzing the decay of γ-H2AX phosphorylation and foci²². RUVBL1 (also known as Pontin), participates in chromatin remodeling and modulates the stability of DDR protein complexes, thus influencing the dephosphorylation of γ-H2AX²³.

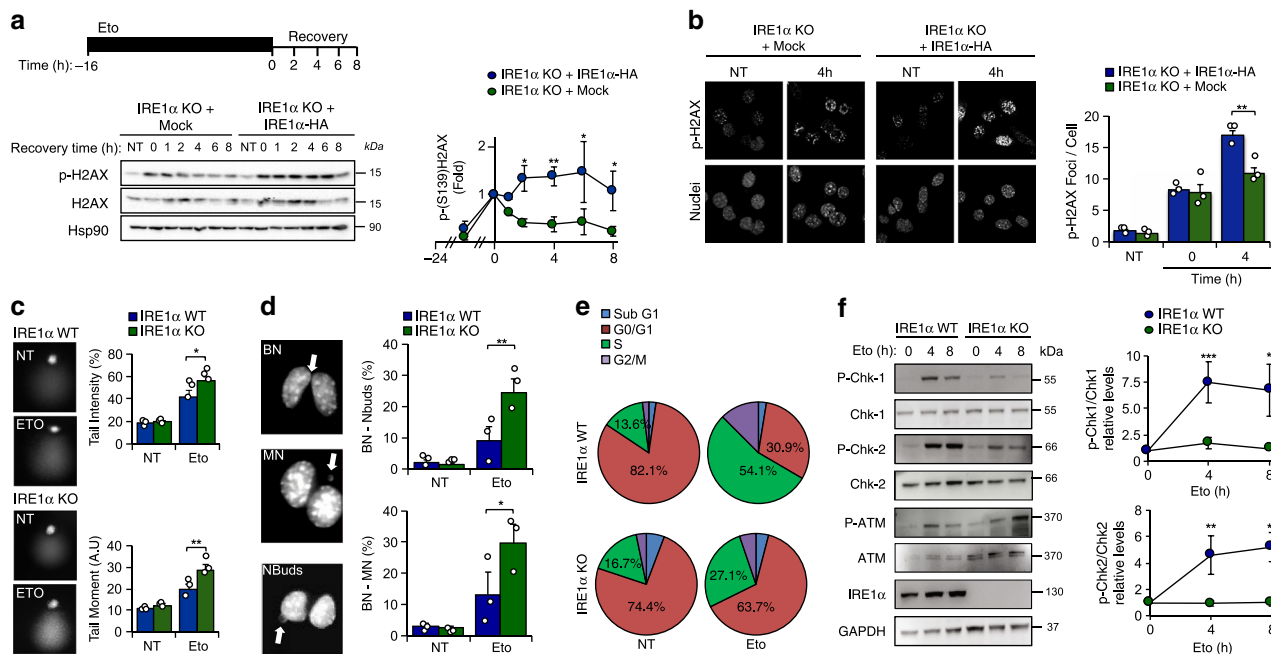


Fig. 2 IRE1 α deficiency impairs the DDR. **a** IRE1 α KO (Mock) and IRE1 α -HA reconstituted cells were pre-incubated with 1 μ M etoposide (Eto) for 16 h and washed three times with PBS and fresh cell culture media was added. The decay of phosphorylated H2AX (P-H2AX) was monitored over time by western blot (middle panel). Quantification of the levels of P-H2AX in cells stimulated with Eto (bottom panel) ($n = 3$). **b** IRE1 α KO (Mock) and IRE1 α -HA reconstituted cells were incubated with 10 μ M Eto for 2 h and then washed with PBS and fresh culture media was added. The distribution P-H2AX expression (green) was monitored by indirect immunofluorescence using confocal microscopy. Nuclei were staining with DAPI (Blue). Quantification of P-H2AX per cell is shown (right panel) ($n = 3$). **c** WT and IRE1 α KO MEFs cells were treated with 10 μ M Eto for 3 h to perform the comet assay. Quantification of tail intensity and tail moment (Tail intensity \times tail area) is shown (right panel) ($n = 3$). **d** WT and IRE1 α KO MEFs cells were treated with 5 μ M Eto for 3 h to determined cytokinesis-block micronucleus cytome assay (CBMC). Binucleated cells (BN) with micronucleus (MN), nuclear buds (NBuds) or nucleoplasmic bridges (NPB; see arrows) were visualized and quantified using epifluorescence microscopy ($n = 3$). **e** WT and IRE1 α KO MEFs cells were treated with 10 μ M Eto for 8 h and cell cycle was analyzed by propidium iodide (PI) staining. Quantification of the percentage of cells in G0/G1 and S phases is shown. **f** WT and IRE1 α KO MEFs cells were treated with 10 μ M Eto for indicated times. Expression and phosphorylation levels of indicated proteins involved in the DDR were monitored by western blot (left panel). Quantification of the levels of p-CHK1 and p-CHK2 is shown (right panel) ($n = 3$). In all panels, data is shown as mean \pm s.e.m.; * $p < 0.05$, ** $p < 0.01$, and *** $p < 0.001$, based on (**a**, **c**, **d**, **f**) two-way ANOVA followed Bonferroni's test, **b** two-way ANOVA followed Tukey's test. Data is provided as a Source Data file.

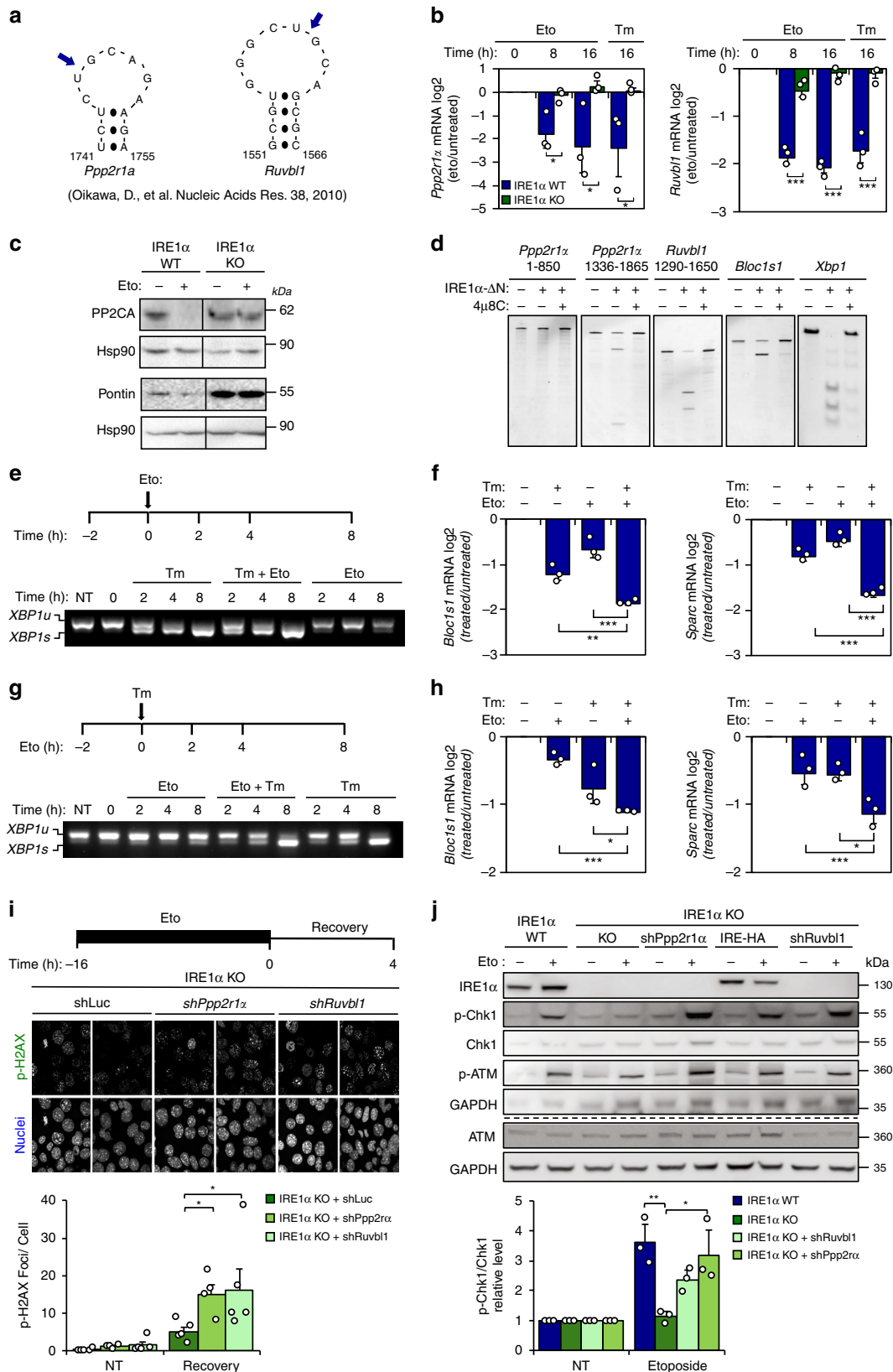
Quantification of *Ppp2r1a* and *Ruvbl1* mRNA levels in cells treated with etoposide demonstrated a decay that was dependent on IRE1 α expression (Fig. 3b). These effects on mRNA levels translated into reduced protein expression of PP2A and RUVBL1 only in wild-type cells exposed to etoposide and the basal upregulation in IRE1 α null cells (Fig. 3c). In a cell-free assay, recombinant IRE1 α directly cleaves a fragment of the *Ppp2r1a* mRNA that contains the RIDD consensus site (spanning nucleotides 1336-1865), but not an adjacent fragment (Fig. 3d). Similarly, IRE1 α exhibited RNase activity on *Ruvbl1* mRNA, thus cleaving this substrate as efficiently as it's known targets *Bloc1s1* mRNA and *Xbp1* mRNA (Fig. 3d). This reaction was suppressed by the IRE1 α inhibitor 4 μ 8C (Fig. 3d).

The lack of *Xbp1* mRNA splicing under DNA damage conditions might involve inhibitory signals, for example mediated by the downregulation of the tRNA ligase RTCB, the targeting of the *Xbp1* mRNA to the ER membrane, or the activity of other regulatory components that are part of IRE1 α clusters and component associated with them²⁴. Analysis of RTCB levels revealed no changes in IRE1 α knockout cells undergoing DNA damage (Supplementary Fig. 4a). To test if DNA damage inhibits *Xbp1* mRNA splicing, we pre-treated cells with tunicamycin for 2 h and then added etoposide at different time points. Remarkably, etoposide failed to interfere with *Xbp1* mRNA splicing induced by tunicamycin (Fig. 3e). Virtually identical results were obtained when a pulse of etoposide was performed followed by the

stimulation of ER stress (Fig. 3g). In contrast, an additive effect was observed on the decay of *Bloc1s1* and *Sparc* mRNAs when ER stress and DNA damaging agents were combined (Fig. 3f, h). These results indicate that DNA damage selectively engages RIDD yet does not cause active suppression of *Xbp1* mRNA splicing.

Considering that PP2A and Pontin are upregulated in IRE1 α null cells under genotoxic stress and are involved in the DDR, we attempted to reverse the phenotype of those cells by depleting *Ppp2r1a* or *Ruvbl1* mRNA with suitable short hairpin RNAs (shRNAs) (Supplementary Fig. 4b). Remarkably, knocking down *Ppp2r1a* or *Ruvbl1* in IRE1 α null cells augmented the levels of phosphorylated γ -H2AX foci after etoposide treatment during the recovery phase (Fig. 3i). Similar results were obtained when phosphorylated γ -H2AX was monitored by immunoblot (Supplementary Fig. 4c). Moreover, knocking-down *Ppp2r1a* and *Ruvbl1* expression in IRE1 α null cells reestablished normal levels of CHK1 phosphorylation (Fig. 3j and Supplementary Fig. 4d, e) and increased population of cells in S/G2M after etoposide treatment (Supplementary Fig. 4f). Taken together, these experiments suggest that the regulation of PP2A and Pontin by IRE1 α contributes to DDR signaling under genotoxic treatment.

c-Abl triggers IRE1 α activation under DNA damage. Recent studies suggest that IRE1 α activation can occur independently from ER stress, impacting various biological processes including



cell migration, synaptic plasticity, angiogenesis and energy metabolism^{14,24,25}. However, until now there are no examples for a selective activation of RIDD in the absence of *Xbp1* mRNA splicing. The release of the ER chaperone BiP from the luminal

domain of IRE1α correlates with its activation under ER stress⁴. Co-immunoprecipitation experiments indicated that the BiP-IRE1α interaction decrease after etoposide treatment, but in a lesser extent than ER stress (Supplementary Fig. 5a).

Fig. 3 IRE1 α controls the stability of mRNAs involved in the DDR. **a** Putative IRE1 α cleavage sites on the *Ppp2r1a* and *Ruvbl1* mRNAs (blue arrows). **b** WT and IRE1 α KO MEF cells were treated with 10 μ M etoposide (Eto). *Ppp2r1a* and *Ruvbl1* mRNA levels were monitored by real-time-PCR. Treatment with 500 ng/mL tunicamycin (Tm) as positive control ($n = 3$). **c** Cells were treated with 10 μ M Eto (16 h) and PP2A and Pontin expression were monitored by western blot ($n = 3$). **d** In vitro RNA cleavage assay was performed using mRNA fragments of human *Ppp2r1a* and *Ruvbl1*, incubated in the presence or absence of recombinant cytosolic portion of IRE1 α (IRE1 α - Δ N) protein (30 min). Experiments were performed in presence or absence of IRE1 α inhibitor 4 μ 8C. *Blos1c1* and *Xbp1* mRNA were used as positive controls. **e** Experimental setup (upper panel): MEF cells were pretreated with 100 ng/mL Tm for 2 h and then treated with 10 μ M Eto. *Xbp1* mRNA splicing was monitored by RT-PCR (bottom panel). **f** RIDD activity was monitored in samples described in **e** ($n = 3$). **g** Experimental setup (upper panel): MEF WT cells were pretreated with 10 μ M Eto for 2 h and then treated with 100 ng/mL Tm. *Xbp1* mRNA splicing was monitored by RT-PCR (bottom panel). **h** RIDD activity was monitored in samples described in **g** ($n = 3$). **i** IRE1 α KO MEF cells were transduced with lentiviruses expressing shRNAs against *Ppp2r1a* (sh*Ppp2r1a*), *Ruvbl1* (sh*Ruvbl1*) or luciferase (sh*Luc*). Cells were incubated with 1 μ M Eto (16 h), washed three times with PBS and fresh media was added. P-H2AX levels were monitored by immunofluorescence after 4 h. P-H2AX foci quantification is shown (Bottom panel) (>200 cells, $n = 4-5$). **j** WT, IRE1 α KO and reconstituted with IRE1 α -HA, expressing sh*Ruvbl1*, sh*Ppp2r1a* or sh*Luc* cells were treated with 5 μ M Eto for 8 h and P-CHK1 and P-ATM monitored by western blot. P-CHK1 quantification is shown (bottom panel) ($n = 3$). All panels data is shown as mean \pm s.e.m.; * $p < 0.05$, ** $p < 0.01$, and *** $p < 0.001$, based on **b** two-way ANOVA followed Bonferroni's test, (**f**, **h-j**) One-way ANOVA followed Tukey's test. Data is provided as a Source Data file.

We then explored possible signaling events that may link the DDR with the induction of RIDD. Interestingly, a recent report indicated that the non-receptor c-Abl tyrosine kinase physically interacts with IRE1 α under metabolic stress, allosterically inducing its oligomerization into a conformation that is more likely to catalyze RIDD than *Xbp1* mRNA splicing²⁶. Of note, c-Abl has been extensively associated to the DDR, regulating cell-cycle arrest and apoptosis²⁷. We confirmed the activation of c-Abl under genotoxic stress (Supplementary Fig. 5b). Treatment of cells with the c-Abl inhibitor imatinib reduced the decay of *Ruvbl1* mRNA in cells exposed to tunicamycin or etoposide (Supplementary Fig. 5c, d). Furthermore, knocking down the expression of c-Abl using shRNAs (Supplementary Fig. 5e) had no effects on the levels of *Xbp1* mRNA splicing (Fig. 4a), but fully prevented the decay of *Ruvbl1* and *Ppp2r1a* mRNAs under ER stress or DNA damage (Fig. 4b), phenocopying the consequences of IRE1 α deficiency. Consistent with these results, imatinib treatment attenuated the generation of IRE1 α -GFP positive clusters in HEK293 cells undergoing genotoxic stress (Fig. 4c, d). Moreover, we also generated a set of c-Abl null MEF cells using the CRISPR/CAS9 technology (Fig. 4e). The deletion of c-Abl prevented the decay of *Ruvbl1*, *Ppp2r1a* (Fig. 4f) and *Bloc1s1* mRNAs, without an effect on the levels of *Xbp1* mRNA splicing (Supplementary Fig. 5f-g). These observations correlated with the formation of a protein complex between IRE1 α and c-Abl as monitored using co-immunoprecipitation in 293T HEK cells overexpressing the proteins (Fig. 4g). We confirmed these results using Proximity Ligation Assay of endogenous c-Abl and IRE1-HA at basal conditions (Fig. 4h) or after exposure to etoposide (Supplementary Fig. 5h, i). Furthermore, using a cell free system, we assessed the effects of recombinant c-Abl on the oligomerization status of purified cytosolic domain of IRE1 α . Incubation of purified IRE1 α at 37 °C induced its spontaneous oligomerization, which was further enhanced when c-Abl was present in the reaction (Fig. 4i). Taken together, these results suggest that the activation of c-Abl in cells undergoing DNA damage contributes to the selective engagement of RIDD, possibly through a direct interaction with IRE1 α .

IRE1 α protect flies against genotoxic stress. To test the possible role of IRE1 α in the maintenance of genome integrity in vivo, we took advantage of *D. melanogaster* as a model organism. The GAL4/UAS system was employed to knockdown the fly orthologue of IRE1 (*dIre1*) using RNAi transgenic animals (Supplementary Fig. 6a). Etoposide treatment failed to trigger an increase in the levels of *dXbp1s* mRNA in larval tissue, as monitored by real time PCR (Fig. 5a). However, larvae fed with etoposide or

tunicamycin exhibited a similar reduction in the mRNA levels of *dSparc* and *dMys*, two well-known RIDD targets in flies²⁸, in addition to *dPontin*, fly orthologue of *Pontin* (Fig. 5b). *dIre1* depletion ablated the downregulation of *dSparc*, *dMys* and *dPpp2r1a*, confirming the occurrence of RIDD (Fig. 5b). Moreover, we then determined the impact of *dIre1* on the survival of animals under genotoxic conditions and quantified the number of larvae reaching adulthood. Knock-down of *dIre1* generated a hypersensitivity phenotype, meaning that most etoposide-treated animals died before reaching maturity (Fig. 5c). Next, we determined the participation of *dIre1* in the maintenance of genome integrity. To this end, we performed the somatic mutation and recombination test (SMART). This assay is based on the induction of mutant spots (clones) that arise from loss of heterozygosity in cells of developing animals, which are heterozygous for a recessive wing cell marker mutation (Supplementary Fig. 6b) generating a multiple wing hair (mwh) phenotype (Fig. 5d, left panel). We expressed a *dIre1* RNAi construct in the wing imaginal disc using a Nubbin-Gal4 driver (Nub-Gal4). Exposure to doxorubicin increased the number of mutant spots in the fly wing, and this phenotype was exacerbated upon depletion of *dIre1* (Fig. 5d, right panel), suggesting compromised DNA repair. Doxorubicin also caused higher rates of apoptosis-associated caspase-3 activation upon *dIre1* knockdown (Fig. 5e). Next, we developed a mosaic analysis to ablate *dIre1* expression with a repressible cell marker (MARCM), a strategy that allows the comparison of wild-type and mutant cells in the same tissue by assessing GFP expression (Supplementary Fig. 6c). Using this mosaic technology, we generated mutant clones for *dIre1* in the eye-antenna imaginal disc and determined the frequency of GFP-positive (*dIre1* null cells) and negative cells (WT cells) that persist in the tissue after etoposide treatment. While *dIre1* expressing cells maintained their viability after exposure to etoposide (Fig. 5f, left panels), *dIre1* null cells proved highly susceptible to this genotoxic agent (Fig. 5f, right panels). Taken together, these results indicate that the fly orthologue of IRE1 α protects against genotoxic stress in vivo.

IRE1 α deficiency impairs the DDR in mice. We then moved forward and investigated the significance of IRE1 α expression to the DDR in vivo and deleted the RNase domain of IRE1 α in the liver and bone marrow using a conditional knockout (cKO) system controlled by the Mx-Cre system²⁹. Poly[I:C] was injected to induce Cre expression, and three weeks later animals were treated with a single dose of either etoposide or tunicamycin, followed by the analysis of liver tissue. A well-established mammalian model of ER stress consists in the intraperitoneal injection

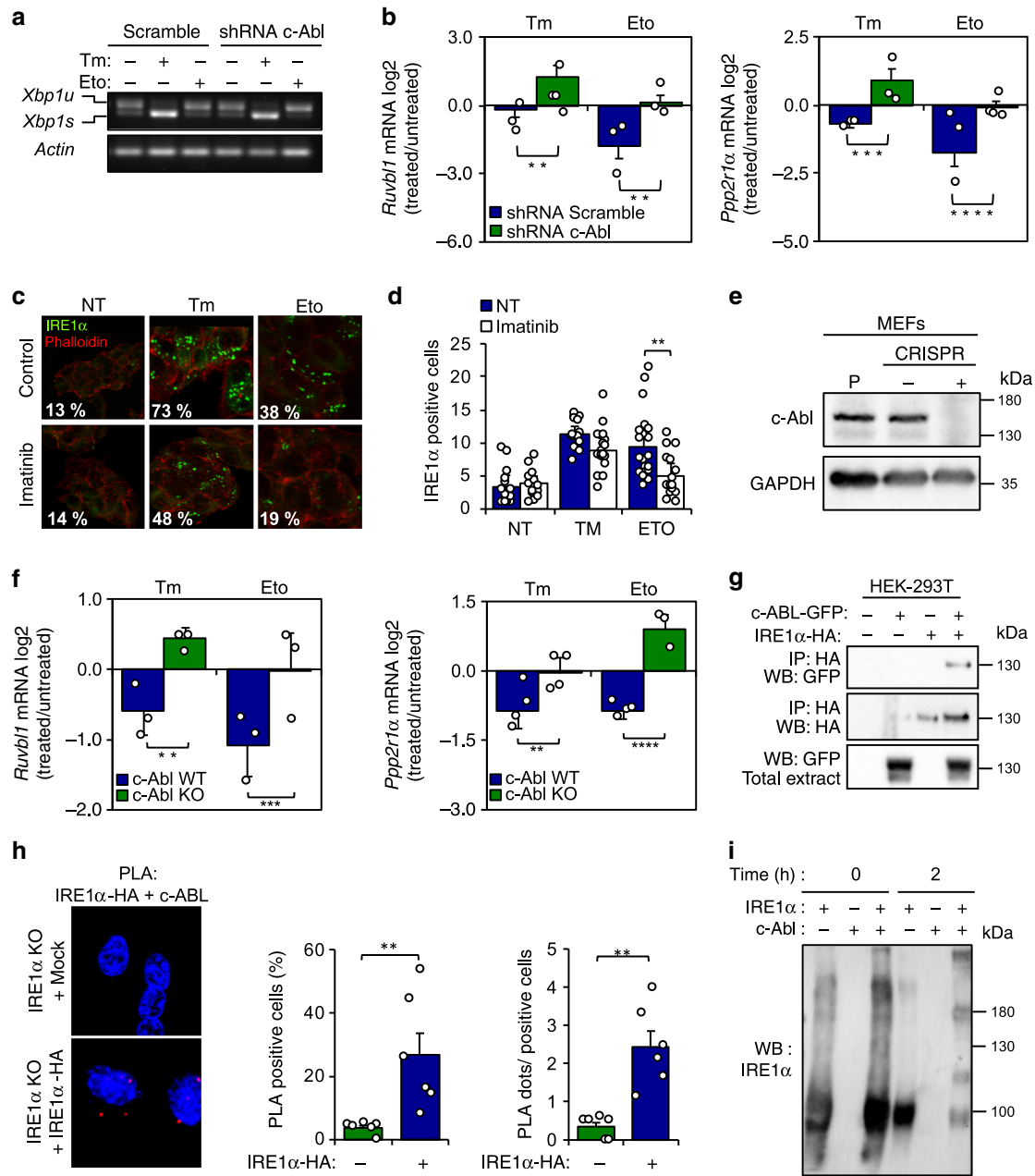


Fig. 4 c-Abl contributes to the RIDD activation under DNA damage. **a** c-Abl was knocked down through the stable delivery of an shRNA. Then cells were treated with 10 μ M Etoposide (Eto) or 500 ng/mL tunicamycin (Tm) for 8 h and *Xbp1* mRNA splicing was monitored by RT-PCR ($n = 3$). **b** MEF ShRNA Scramble and ShRNA c-Abl cells were treated with 10 μ M Eto or 500 ng/mL Tm for 8 h, and the decay of *Ppp2r1a* and *Ruvb1* was measured by real-time-PCR ($n = 3$). **c** Trex-IRE1-GFP cells were pre-treated with 10 μ M imatinib by 1 h, and then treated with 10 μ M Eto, or 500 ng/mL Tm for 8 h and IRE1-GFP foci visualized by confocal microscopy. **d** Quantification of the percentage of cells positive IRE1-GFP clusters is shown (>200 cells, $n = 3$). **e** c-Abl expression in CRISPR control and c-Abl KO cells was monitored by western blot ($n = 3$). **f** CRISPR control and c-Abl KO cells were treated with 10 μ M Eto or 500 ng/mL Tm for 8 h, and the decay of *Ruvb1* and *Ppp2r1a* was measured by Real-Time-PCR ($n = 3$). **g** HEK-293T cells reconstituted with IRE1 α -HA and c-Abl-GFP were exposed to 10 μ M Eto for 8 h. Immunoprecipitation (IP) was performed using the HA epitope (IRE1 α) and GFP (c-Abl) to assess the possible interaction with c-Abl. **h** IRE1 α KO (Mock) and reconstituted cells with an IRE1 α -HA were treated 8 h with 10 μ M Eto and stained with a proximity ligation assay (PLA) using an anti-HA or anti-c-Abl antibodies and analyzed by confocal microscopy. Right panel: Number of dots per cell analyzed and percentage of PLA positive cells were quantified ($n = 6$). **i** Recombinant IRE1 α and c-Abl proteins were incubated at indicated time points and assess its possible interaction by western blot. All data represents the mean \pm s.e.m. of three independent experiments, except for co-IP that were performed twice. * $p < 0.05$, ** $p < 0.01$, and *** $p < 0.001$, based on (**b, f**) two-way ANOVA followed Bonferroni's test, (**d, h**) One-way ANOVA followed Tukey's test. Data is provided as a Source Data file.

of tunicamycin, which elicits a rapid stress response in the liver. Although evident signs of DNA damage were observed in both control and IRE1 α ^{CKO} animals (indicated by a rise in *p21* mRNA) (Fig. 6a upper panel and Supplementary Fig. 7a), no *Xbp1* mRNA

splicing was detected in the etoposide treated group (Fig. 6a, bottom panel). In sharp contrast, a clear down-regulation of *Ppp2r1a* and *Bloc1s1* mRNA levels occurred in the livers (Fig. 6b) and bone marrows (Supplementary Fig. 7b) from control (but not

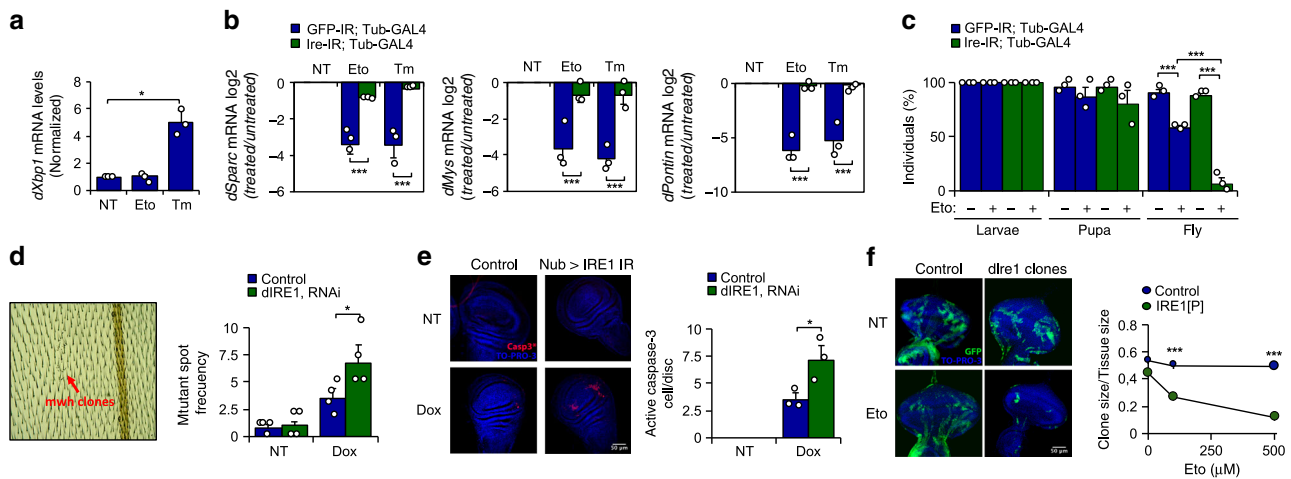


Fig. 5 IRE1 α expression confers protection against genotoxic stress in fly models. **a** *D. melanogaster* larvae were fed with 100 μ M etoposide (Eto) or 50 μ g/ml tunicamycin (Tm) for 4 h and then *dXbp1s* mRNA evaluated by real-time PCR and normalized to the expression levels of *dRpl32* gene ($n = 3$). **b** *dlre1* mRNA was knocked down by expressing a specific RNAi constructs under the control of tubulin-Gal4 driver. *D. melanogaster* larvae were fed with 100 μ M Eto or 50 μ g/ml Tm for 4 h and the decay of RIDD targets *dSparc*, *dPontin*, and *dMys* mRNA was evaluated by RT-qPCR and normalized to the expression levels of *dRpl32* mRNA ($n = 3$). **c** Control and *dlre1* knockdown larvae were fed with 500 μ M Eto and allowed to reach adulthood for survival analysis. The number of hatched flies was quantified ($n = 20$ per group) ($n = 3$). **d** A *dlre1*-RNAi expressing fly line was generated to specifically target *dlre1* in the imaginal disc of *D. melanogaster*. The wing SMART assays test was used to monitor genomic alterations after targeting *dlre1* in flies. Larvae in first instar were grown in food supplemented with the DNA damaging agent 0.125 mg/ml doxorubicin (Dox) or 0.5% DMSO as control. Adult flies from control and *dlre1* RNAi larvae were fixed and the left wing analyzed for the number of mwh clones (right panel) ($n = 3$). **e** Using the same experimental setting described in **d**, imaginal discs were collected, fixed and caspase-3 positive cells detected by immunofluorescence. Nucleus was stained with TO-PRO3 to visualize total number of cells. Quantification of active caspase-3 cells per imaginal disc is presented (right panel) ($n = 3$). **f** Mutant knockout *dlre1* cells (*dlre1* clone) in the eye-antenna imaginal disc were marked with GFP (see methods). Quantification of the ratio clone size/disc size is presented (right panel) ($n = 10$ clones). In all panels, data is shown as mean \pm s.e.m.; * $p < 0.05$, ** $p < 0.01$, and *** $p < 0.001$, based on **a** one-way ANOVA followed Tukey's test, **b-f** two-way ANOVA followed Bonferroni's test. Data is provided as a Source Data file.

IRE1 α -deficient) animals injected with etoposide. Again, no *Xbp1* mRNA splicing was detected in the etoposide treated group, whereas exposure of animals to tunicamycin triggered a very mild response in bone marrow tissue (Supplementary Fig. 7c). In addition, IRE1 α deficiency in the liver altered the DDR, reflected in reduced phosphorylation of CHK1 in animals injected with etoposide (Fig. 6c). Importantly, ablation of IRE1 α resulted in enhanced susceptibility of liver cells to apoptosis measured as enhanced caspase-3 activation (Fig. 6d).

Finally, to assess the significance of IRE1 α to the DDR on an unbiased manner, we performed a gene expression profile analysis of liver tissue derived from mice exposed to etoposide or tunicamycin. Pathway enrichment analysis indicated that IRE1 α deficiency attenuated the establishment of a global DDR, delayed the expression of cell cycle arrest genes and activated proapoptotic pathways (Fig. 6e and Supplementary Fig. 8a). As expected, under ER stress induced by tunicamycin, IRE1 α deficiency in the liver significantly impacted the expression of genes involved in proteostasis control in the secretory pathway (trafficking, folding and quality control) (Supplementary Fig. 8b, c). Taken together, these findings demonstrate that IRE1 α signaling contributes to maintaining the stability of the genome when cells face DNA damage.

Discussion

The current study supports a conserved function for IRE1 α as a signaling module of the DDR that differs from its canonical role as an UPR mediator. We propose that IRE1 α is part of a key decision-making node in a complex interplay between cell survival and DNA repair upon genotoxic stress. In this context, IRE1 α regulates the levels of PP2A and RUVBL1 through the selective engagement of RIDD, controlling the kinetics and

amplitude of γ -H2AX phosphorylation. The contribution of IRE1 α to genome stability is conserved in evolution from insects to mammals and impacts whole animal survival as demonstrated using flies. Our results suggest a regulatory mechanism in which the RNase domain of IRE1 α is selectively regulated to specifically engage RIDD, presumably upon interaction with c-Abl (Fig. 4g, h). This view is consistent with recent studies that connected using unbiased approaches the pathways involved in maintenance of genome integrity and proteostasis, showing that dysregulation of the DDR resulted in protein aggregation and autophagy induction^{30,31}. Moreover, previous work demonstrated that the function and structure of the ER is drastically affected by DNA damaging agents used in chemotherapy^{32,33}. Other recent reports suggested that chronic ER stress suppresses DNA repair and sensitizes cancer cells to ionizing radiation and chemotherapy^{34–37}, in addition to enhancing oxidative damage to the DNA³⁸. Interestingly, a recent study also reported that XBP1u, the protein encoded by the unspliced version of *Xbp1* mRNA, regulates the stability of TP53, suggesting alternative connections between the UPR and the DDR under resting conditions³⁹. Our results suggest that IRE1 α specifically affects signaling events regulating the DDR, and not the DNA damage sensing process. IRE1 α operates as an amplification loop, impacting the sustained activation of CHK1/2 and the phosphorylation of γ -H2X through the control of the RIDD targets *Ppp2r1a* and *Ruvb1l*, leading to cell cycle arrest and improved DNA repair and as a consequence maintenance of cell survival (see working model in Fig. 6f).

Although RIDD is proposed to be necessary for the maintenance of ER homeostasis^{8,10} and to contribute to the pathogenesis of diabetes⁵, cancer^{40,41}, and inflammatory conditions^{42–44}, most of the available evidence is difficult to interpret due to the concomitant existence of *Xbp1* mRNA splicing. Our study supports a fundamental biological function for RIDD in the maintenance of

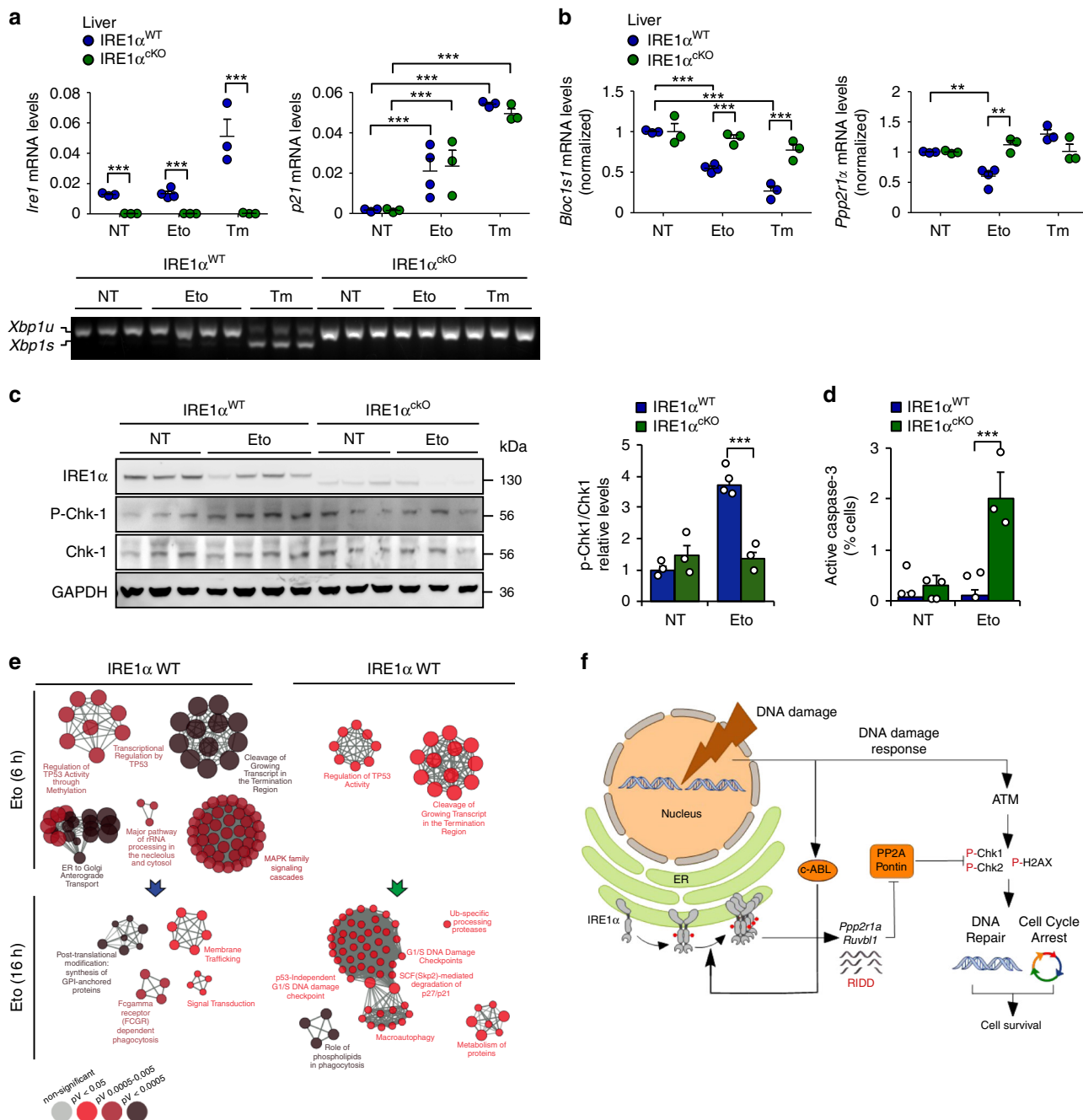


Fig. 6 IRE1 α deletion in liver alters the DDR under genotoxic stress. **a** IRE1 α was conditionally deleted the liver using the MxCre and LoXP system (IRE1 α^{cKO}). Mice were intraperitoneally injected with 50 mg/Kg etoposide (Eto) or 1 mg/Kg tunicamycin (Tm) and sacrificed 6 h and 16 h later. Total mRNA levels of the deleted *IRE1*, and *p21* were measured 6 h later in the liver by real-time-PCR ($n = 3-4$ mice per group). *Xbp1* mRNA splicing (bottom panel) was monitored in the same samples by RT-PCR. **b** Liver extracts of animals described in **a**, *Ppp2r1a* and *Bloc1s1* mRNA expression levels were measured 6 h later of Eto treatment by real-time-PCR ($n = 3$). **c** Protein liver extracts were obtained from mice treated described in **a** and the expression levels of indicated proteins were monitored 6 h later of Eto treatment by western blot. Quantification of the levels of p-CHK1 is shown (Right panel). **d** Mice from **a** were intraperitoneally injected with 50 mg/Kg Eto and sacrificed 48 h later. Then, livers active-caspase 3 detected by immunohistochemistry ($n = 2-3$). **e** Gene expression profile analysis was performed in mRNA from liver extracts of animals described in **a**. Most significant pathways altered by Eto administration in WT and IRE1 α null livers are shown. Three independent biological samples were used. In all panels, data is shown as mean \pm s.e.m.; * $p < 0.05$, ** $p < 0.01$, and *** $p < 0.001$, based on **a-d** two-way ANOVA followed Bonferroni's test. Data is provided as a Source Data file. **f** Working model: genotoxic stress activates IRE1 α in the absence of ER stress markers, selectively engaging RIDD. IRE1 α degrades mRNAs involved in the DNA damage response encoding for *Ppp2r1a* and *Ruvbl1*, regulating the (de)phosphorylation of the histone H2AX and CHK-1/2. The non-canonical activation of IRE1 α involves the participation of the c-Abl kinase that is activated by DNA damage response kinases as ATM. The expression and function of IRE1 α is essential to promote survival under DNA damage conditions by controlling cell cycle arrest and DNA repair programs.

genome integrity, representing a unique example for a selective and specific activation of RIDD with clear physiological implications. IRE1 α is frequently affected by loss-of-function mutations in cancer^{2,45}, contrasting with the notion that cancer cells require IRE1 α to survive in hypoxic conditions^{3,6}. Our present results support the idea that the genetic alterations of IRE1 α observed in cancer may synergize with oncogenes to promote genomic instability due to inefficient DNA repair. Altogether, we uncovered a previously unanticipated function of a major UPR signal transducer as an integral component of the DDR, revealing an intimate connection between the pathways that assure the integrity of the proteome and the genome.

Methods

Reagents. Etoposide, doxorubicin, 5-fluorouracil, hydroxyurea, imatinib and 4 μ 8C were purchased from Sigma Aldrich. Tunicamycin was obtained from Calbiochem EMB Bioscience Inc. IRE1 inhibitor MKC-8866 was provided by Dr. John Patterson (Fosun Orinove). Cell culture media, fetal calf serum, and antibiotics were obtained from Life Technologies and Sigma Aldrich. Fluorescent probes and secondary antibodies coupled to fluorescent markers were purchased from Molecular Probes, Invitrogen. All other reagents were obtained from Sigma or the highest grade available.

Cell culture and DNA constructs. All MEF and HEK cells used here were maintained in Dulbecco's modified Eagles medium supplemented with 5% fetal bovine serum, non-essential amino acids and grown at 37 °C and 5% CO₂. IRE1 α deficient cells were previously described²⁵. The production of amphotropic retroviruses using the HEK293GPG packing cell line was performed as described in ref. ⁴⁶. Retroviral plasmids were transfected using Efectene (Qiagen, Valencia, CA, USA) according to the manufacturer's protocols. IRE1 α -HA expressing retroviruses were previously described in the pMSCV-Hygro vector⁴⁶, where IRE1 α contains two tandem HA sequences at the C-terminal domain and a precision enzyme site before the HA tag.

RNA isolation, RT-PCR and real time PCR. Total RNA was prepared from cells and tissues using Trizol (Invitrogen, Carlsbad, CA, USA), and cDNA was synthesized with SuperScript III (Invitrogen) using random primers p(dN)6 (Roche). Quantitative real-time PCR reactions were performed using SYBRgreen fluorescent reagent and/or EvaGreenTM using a Stratagene Mx3000P system (Agilent Technologies, Santa Clara, CA 95051, United States). The relative amounts of mRNAs were calculated from the values of comparative threshold cycle by using *Actin* as a control and *Rpl19* or *Rpl32* for RIDD substrates in mouse or *D. melanogaster* samples, respectively. All methods for *Xbp1* mRNA splicing assay were previously described in ref. ⁴⁷ using primers described in Supplementary Table 1.

Immunoprecipitations. HEK-293T cells reconstituted with IRE1 α -HA and c-Abl-GFP and IRE1 α deficient MEF cells stably transduced with retroviral expression vectors for IRE1 α -HA or empty vector were incubated in presence or absence of tunicamycin (500 ng/mL for 4 h) or etoposide (10 μ M for 16 h). Cell lysates were prepared for immunoprecipitations in lysis buffer (0.5% NP-40, 50 mM NaCl, 50 mM Tris pH 7.6, 50 mM NaF, 1 mM Na₃VO₄ and protease inhibitors). Immunoprecipitations (IP) were performed as described⁴⁸. In brief, to IP HA-tagged IRE1 α , protein extracts were incubated with anti-HA antibody-agarose complexes (Roche), for 4 h at 4 °C, and then washed three times with 1 mL of lysis buffer and then one time in lysis buffer with 350 mM NaCl. Beads were dried and resuspended in Sample Buffer 2x. Samples were heated for 5 min at 95 °C and resolved by SDS-PAGE 8% followed by western blot analysis.

Western blot analysis. Cells were collected and homogenized in RIPA buffer (20 mM Tris pH 8.0, 150 mM NaCl, 0.1% SDS, 0.5% Triton X-100) containing a protease inhibitor cocktail (Roche, Basel, Switzerland) in presence of 50 mM NaF and 1 mM Na₃VO₄. Protein concentration was determined in all experiments by micro-BCA assay (Pierce, Rockford, IL), and 20–40 μ g of total protein was loaded onto 8–12% SDS-PAGE minigels (Bio-Rad Laboratories, Hercules, CA) prior transfer onto PVDF membranes. To evaluate IRE1 α phosphorylation, SDS-PAGE minigel were made in presence of the 5 μ M of Phostag reagent and 10 μ M MnCl₂. Membranes were blocked using PBS, 0.1% Tween-20 (PBST) containing 5% milk for 60 min at room temperature then probed overnight with primary antibodies. The following antibodies diluted in blocking solution were used in this study: anti-BiP 1:1000 (Abcam, Cat. ab21685); Anti-phosphorylated S139-H2AX 1:5000 (Millipore, Cat. 05-636), anti-DDIT3 (CHOP) 1:1000 (Santa Cruz, Cat. sc-575), anti-XBP1s 1:1000 (Santa Cruz, Cat. 7160), anti-ATF4 1:2000 (Santa Cruz, Cat. sc-200), anti-Hsp90 1:5000 (Santa Cruz, Cat. sc-13119), anti-IRE1 α (14C10) (Santa Cruz, Cat. 3294), anti-Chk1 1:1000 (Santa Cruz, Cat. sc-8408), anti-Chk2 1:1000 (Santa Cruz, Cat. sc-17747), anti-phosphorylated-Chk2, Thr68 1:1000 (Santa Cruz, Cat. sc-16297-R), anti-ATM 1:1000 (Santa Cruz, Cat. sc-7129), anti-HA 1:1000

(Roche, Cat. 11666606001), anti-PP2A A 1:1000 (Cell Signaling technology, Cat. 2041S), anti-RuvbL1 1:1000 (Cell Signaling technology, Cat. 12300), anti-eIF2 α 1:1000 (Cell Signaling technology, Cat. 9722), anti-phosphorylated-eIF2 α 1:1000 (Cell Signaling technology, Cat. 9721), anti-PERK 1:1000 (Cell Signaling technology, Cat. 3192), anti-IRE1 α 1:1000 (Cell Signaling technology, Cat. 3294), anti-phosphorylated-Chk1, Ser348 1:1000 (Cell Signaling, Cat. 2341), anti-HA 1:1000 (Cell Signaling, Cat. 3724), anti-GAPDH 1:1000 (Cell Signaling, Cat. 21185), anti-Abl 1:1000 (Sigma, Cat. A5844), anti-phosphorylated-c-Abl, pTyr412, 1:1000 (Sigma, Cat. C52490), anti-SMC1 1:1000 (Abcam, ab21583), anti-phosphorylated-SMC1, Ser957, 1:1000 (Abcam, ab137871), anti-KAP1, 1:1000 (Abcam, ab190178), anti-phosphorylated-KAP1, Ser824, 1:1000 (Abcam, ab70369), anti-phosphorylated-ATM Ser 198 1:1000 (MERK, Cat. 05-740), anti-p21 (Santa Cruz, Cat. sc-6246), anti-phospho-p53 (Cell Signaling, Cat. 9286 S), anti-p53 (Santa Cruz, Cat. sc-98), anti-p53 (Santa Cruz, Cat. sc-55476). Bound antibodies were detected with peroxidase-coupled secondary antibodies incubated for 1 h at room temperature and the ECL system.

IRE1 α oligomerization assay. TREX cells expressing IRE1 α -3F6HGFP WT were obtained from Dr. Peter Walter at UCSF and were previously described¹³. TREX cells plated and treated with doxycycline (500 ng/mL for 48 h). Cells were treated with Tm (1 μ g/mL) or etoposide (25 μ M) for different times points and fixed with 4% paraformaldehyde for 30 min. Nuclei were stained with Hoechst dye. Coverslips were mounted with Fluoromount G onto slides and visualized by confocal microscopy (Fluoview FV1000). The number and size of IRE1 α foci was quantified using segmentation and particle analysis of Image J software.

In vitro oligomerization assay. In all, 0.5 μ g of the cytoplasmic domain of GST-tagged IRE1 α (Sino Biologicals) and 0.1 μ g of His tagged c-Abl (Carna Biosciences) were incubating and mixing for indicated time points, at 37 °C in a heat block (300 rpm). Total reaction was prepared in 100 μ L of oligomerization assay buffer (50 mM Tris-HCl pH 7.5, 100 mM NaCl, 5 mM MnCl₂, 5 mM MgCl₂, 1 mM DTT, 1 mM ATP). The half of the reaction mixture was mixed with NuPAGE LDS sample buffer (Invitrogen) and loaded on 6% denaturing polyacrylamide gel and subsequently analyzed by western blot.

Indirect Immunofluorescence. IRE1 α -HA, and γ -H2AX proteins were visualized by immunofluorescence. Cells were fixed for 30 min with 4% paraformaldehyde and permeabilized 0.5% NP-40 in PBS containing 0.5% BSA (bovine serum albumin) for 10 min. After blocking for 1 h with 10% FBS in PBS containing 0.5% BSA, cells were subsequently incubated with anti-HA 1:1000 (Invitrogen, Cat. 715500), anti-phosphorylated-Chk1, Ser348 1:1000 (Cell Signaling, Cat. 2341), anti-cleaved caspase 3, Asp175 1: (Cell Signaling, Cat. 9661) or anti-Phosphorylated S139-H2AX 1:5000 (Millipore, Cat. 05-636) antibodies overnight at 4 °C. Cell were washed three times in PBS containing 0.5% BSA, and incubated with Alexa-conjugated secondary antibodies (Molecular Probes) for 1 h at 37 °C. Nuclei were stained with Hoechst dye. Coverslips were mounted with Fluoromount G onto slides and visualized by confocal microscopy (Fluoview FV1000).

Automated microscopy. Cells were seeded in 96-well imaging plates (BD Falcon, Sparks, USA) 24 h before stimulation. Cells were treated with the indicated agents. Subsequently, cells were fixed with 4% PFA and counterstained with 10 μ M Hoechst 33342. After blocking for 1 h with 10% FBS in PBS containing 0.5% BSA, cells were subsequently incubated with anti-phosphorylated-Chk1, Ser345 1:1000 (Cell Signaling, Cat. 2348) antibody, overnight at 4 °C. Cell were washed three times in PBS, and incubated with Alexa-conjugated secondary antibodies (Molecular Probes) for 1 h at 37 °C. Images were acquired using an ImageXpress Micro XLS Widefield High-Content Analysis System operated by the MetaXpress® Image Acquisition and Analysis Software (Molecular Devices, Sunnyvale, CA, US). Acquisition was performed by means of a 20X PlanApo objective (Nikon, Tokyo, Japan). Minium 9 views fields per well for 96-wells plate were acquired. MetaXpress® was utilised to segment cells into nuclear area (based on Hoechst 33342 signal). Cell-like objects were segmented and divided into cytoplasmic and nuclear regions as previously reported⁴⁹.

Proximity ligation assay (PLA). Cells were seeded in 12 mm cover slips. After the indicated treatments, cells were fixed for 20 min at RT with 4% paraformaldehyde and permeabilized 0.5% NP-40 in PBS containing 0.5% BSA (Bovine serum albumin) for 10 min. After blocking for 1 h with 10% FBS in PBS containing 0.5% BSA, cells were incubated with the indicated antibodies: Anti-HA (Cat: 901514, Biologend or Cat: 9110, Abcam) and anti-Abl 1:1000 (Sigma, Cat. A5844) overnight at 4 °C following by Duolink manufacturer's instructions (Duolink®, Sigma-Aldrich). Images were acquired by confocal microscopy (Nikon C2 plus) using a 60X oil objective lens stacking the images every 0.5 μ m to cover all the image of interest. Stack images were deconvoluted using Huygens and ImageJ. Stack deconvoluted images were reduced to one dimension by sumslices function (ImageJ). Colocalization was performed in thresholded and masked images were used to determine Manders/Pearson's index was calculated with ImageJ plugin.

Comet assay. The comet assay was performed as previously described⁵⁰. Briefly, agarose-slides were prepared with 1% low-gelling-temperature agarose and 2×10^4 cells/ml and submerged in lysis solution (1.2 M NaCl, 100 mM Na₂-EDTA, 0.1% sodium lauryl sarcosinate, 0.26 M NaOH (pH > 13)) for 18 h at 4 °C in the dark. Then, carefully slides removed and submerged in room temperature (18 – 25 °C) in rinse solution (0.03 M NaOH, 2 mM Na₂EDTA (pH ~12.3)) for 20 min. electrophoresis was conducted in the same solution for 25 min at a voltage of 0.6 V/cm. Finally, slides were stained in a solution containing 2.5 µg/ml of propidium iodide in distilled water for 20 min and observed in a epifluorescence microscopy. Images were analyzed using Comet Assay IV software.

Cytokinesis-block micronucleus assay. Cytokinesis-block micronucleus (CBMN) assay was performed as previously described⁵¹. In brief, cells were treated with 5 etoposide (5 µM for 3 h). Then, cells were washed three times with PBS and incubated for 24 h with fresh media with 5 µM of Cytochalasin-B. Cells were fixed, stained with Hoechst. Binucleated cells (BN) with micronucleus (MN), Nuclear buds (Nbuds) or nucleoplasmid bridges (NPB) were detected and quantified using epifluorescence microscopy.

In vitro RNA cleavage assay. *Bloc1s1* (NM_001487.3), *Ppp2r1a* (NM_014225) and *RuvbL1* (NM_00370) cDNA were obtained from MGC cDNA library (Dharmacon). Long sense and antisense oligonucleotides containing a minimal T7 RNA polymerase promoter (5'-TAATACGACTCACTATAGG-3') fused upstream of the sequence containing different fragments of the genes *Ppp2r1a*, *RuvbL1* and *Bloc1s1* harboring 5'-EcoRI and 3'-BamHI overhangs were annealed and ligated into the cognate restriction sites of pUC19 (Invitrogen, Life Technologies). Oligonucleotides sequence to clone *Ppp2r1a* and *RuvbL1* fragments were described previously²⁰. In vitro transcription reactions were performed with T7 RNA polymerase using the HiScribe T7 high-yield RNA synthesis kit (New England Biolabs) following the manufacturer's recommendations. The transcribed RNA were treated for 20 min with DNase and purified by urea-polyacrylamide gel electrophoresis (urea-PAGE). RNAs recovered from gel fragments by the crush-and-soak method, were precipitated with 300 mM NaOAc and 1 volume of isopropanol. No co-precipitants were employed. The precipitated RNA pellets were desalted by two washes with 70% ice-cold ethanol, air-dried and re-suspended in an appropriate volume of either nuclease-free water or RNA resuspension buffer (20 mM HEPES, 100 mM NaCl, 1 mM Mg(OAc)₂). The oligonucleotides sequence used are listed in the Supplementary Table 2.

The cytosolic kinase/ribonuclease domain construct of IRE1α (KR43) was expressed and purified as described previously⁵². In vitro transcribed, PAGE-purified, refolded RNAs (50 ng) were incubated with 0.5 µM IRE1α-KR43 for the indicated times in RNA cleavage buffer (20 mM HEPES pH 7.5, 70 mM NaCl, 2 mM Mg(OAc)₂, 1 mM TCEP, and 5% glycerol). Stop solution (10 M urea, 0.1% SDS, 1 mM EDTA, 0.05% xylene cyanol, 0.05% bromophenol blue) was added at five-fold excess to stop the reactions followed by heating at 80 °C for 3 min. The denatured samples were then loaded on 6% TBE-urea gels (Invitrogen, Life Technologies) and the gels stained with SYBR Gold nucleic acid stain (Invitrogen, Life Technologies). As a negative control we utilized the IRE1α inhibitor 4µ8C to a final concentration of 5 µM.

Viability assay. In all, 2.0×10^4 cells were seeded in 48-well plate and the maintained by 24 h in DMEM cell culture media supplemented with 5% bovine fetal serum and non-essential amino acids. Genotoxic and ER stress were induced by adding genotoxic and ER stress agents to the cells at different concentrations, and maintained for 24 h. Then, cell viability was monitored using propidium iodide staining and flow cytometry (BD FACS Canto, Biosciences).

Mouse model. *Ern1* floxed mice were previously described⁵³ and crossed with *Mx1-cre* transgenic mice to generate a conditional KO animal (IRE1α^{CKO}). Deletion was induced by injection of polyinosinic-polycytidylic acid (Poly (I:C)) which efficiently delete the floxed gene in the liver and bone marrow²⁹. In all, 5–6-week-old mice were intraperitoneally (i.p) injected three times with 250 µg of poly(I:C) each time with 2 day intervals to induce the Cre expression. Mice were used for experiments at least 2–3 weeks after the final poly (I:C) injection. DMSO or 50 mg/Kg etoposide or 1 mg/Kg tunicamycin or were i.p. injected and 6 h later mice were sacrificed as reported⁵⁴. The liver and bone marrow were frozen at –80 °C for biochemical analysis and the right major lobe of the liver was placed in a petri dish (on ice). Liver tissue was washed in PBS to remove the blood and then, it was fixed in 4% paraformaldehyde (72 h) for histological analyses. The animals' works and care was in accordance with institutional guidelines. Institutional Committee for Animal Care and Handling, University of Chile (Protocol CICUA-CBA-0833).

Fly studies. Flies were kept at 25 °C on standard medium with a 12–12 dark–light cycle. Drug administration protocol for all experiments is as follows: Larvae were grown in standard fly medium until day 3 after egg laying (AEL). Then they were transferred to fly instant medium (Carolina Biological Supply 2700 York Burlington, NC, USA) complemented with the appropriate drug for the different treatments. Larvae were fed with the corresponding drug-supplemented media until dissection or adulthood.

The UAS-Ire1 IR (v39562) line was obtained from the Vienna Drosophila RNAi Center (VDRC). The following lines were obtained from Bloomington Drosophila Stock Center (BDSC): UAS-GFP IR (BL-44412); Ire1 mutant w1118; PBac{WH} Ire1¹⁰²¹⁷⁰/TM6B (BL-18520); *mwh*¹ mutant (BL-549) and *flr*³/TM3, Ser stock (BL-2371). All fly strains are listed in the Supplementary Table 3.

SMART assay. For the SMART assay, larvae were fed in media complemented with 0.125 mg/mL Doxorubicin. Wings of the hatched female flies were fixed in ethanol, mounted in ethanol:lactic acid 1:1, and 15 wings per condition were analyzed at $\times 400$ magnification for the occurrence of mutant clones ($N = 4$)⁵⁵.

Survival curve and biochemical analysis of fly tissue. Survival analyses were carried out growing 20 experimental or control larvae in 500 µM etoposide and the number of living animals was quantified at different time points. For real time RT-PCR analysis, total RNA was extracted from third instar larvae (same treatment as the survival analysis animals) using Trizol (Invitrogen, Carlsbad, CA, USA), and cDNA was synthesized with SuperScript III (Invitrogen)^{56,57}.

For immunohistochemistry, larvae were fed with 0.125 mg/mL doxorubicin. Then third instar larvae were dissected and fixed as described previously⁵⁸. Larvae carcasses were incubated with Anti-caspase-3 (1:100, Cell Signaling) overnight in PBT supplemented with 0.5% BSA at 4 °C, washed four times with PBT for 15 min and stained with Alexa-conjugated secondary antibody (1:200, Molecular Probes) and TO-PRO3 (1 µM, Invitrogen). VectaShield (Vector Laboratories, Burlingame, California, USA) was used as a mounting media. The number of active Caspase-3 positive cells was quantified in 10 wing imaginal discs ($N = 3$). Images were taken using a Zeiss LSM510 confocal microscope and analyzed with ImageJ software.

Microarray analyses. Affymetrix gene expression data were pre-processed using Transcriptome Analysis Console (TAC) (v4.0, ThermoFisher Scientific). Custom mouse Brainarray chip definition (v22) was used to further annotate the DE files with Entrez and gene symbol IDs. For further analysis, just gene transcript with FDR ($\alpha = 0.05$) correction and 1.5 > fold change was considered. For pathway enrichment analysis, data obtained from untreated wild type or IRE1α^{CKO} after poly I:C treatment liver mice tissues were used as reference for tunicamycin (Tm) and etoposide (Eto) treatment comparisons, to further input them in ClueGO (v2.3.2) software using Reactome pathway enrichment database (v09.11.2016). In addition, to visualize patterns in the gene expression and pathway enrichment scores for specific ontologies, heatmaps were generated using RStudio (v0.99.489, R 3.4.1) based on KEGG pathway database gene lists. Genes which show change of the ratios higher (or lower) than 1.5-fold in the arrays at any comparison have been considered as up or downregulated and subjected for functional enrichment analysis. The Bioconductor package 'clusterProfiler' was applied to perform functional enrichment analysis using the following repositories: GO (Gene Ontology), KEGG (Kyoto Encyclopedia of Genes and Genomes), and Reactome Pathways. GEO Dataset ID: GSE130952.

Statistical analysis. Results were statistically compared using the Ordinary One-way ANOVA and Two-way ANOVA followed by different multiples comparison post-tests (Tukey's Multiple Comparison Test or Bonferroni's Multiple Comparison Test). When pertinent, Student's *t*-test was performed for unpaired or paired groups. In all plots *p* values are show as indicated: *, $p < 0.05$; **, $p < 0.01$; ***, $p < 0.001$ and ****, $p < 0.0001$ and were considered significant. n.s: non-significant.

Reporting summary. Further information on research design is available in the Nature Research Reporting Summary linked to this article.

Data availability

The source data underlying Figures and Supplementary Figures are provided as a Source Data file. All data is available from the corresponding author upon reasonable request.

Received: 18 April 2019; Accepted: 12 March 2020;

References

- Pearl, L. H., Schierz, A. C., Ward, S. E., Al-lazikani, B. & Pearl, F. M. G. Therapeutic opportunities within the DNA damage response. *Nat. Rev. Cancer* **15**, 166–180 (2015).
- Chevet, E., Hetz, C. & Samali, A. Endoplasmic reticulum stress-activated cell reprogramming in oncogenesis. *Cancer Discov.* **5**, 586–597 (2016).
- Cubillos-Ruiz, J. R., Bettigole, S. E. & Glimcher, L. H. Tumorigenic and immunosuppressive effects of endoplasmic reticulum stress in cancer. *Cell* **168**, 692–706 (2017).

4. Walter, P. & Ron, D. The unfolded protein response: from stress pathway to homeostatic regulation. *Science* **334**, 1081–1086 (2011).
5. Hetz, C. & Papa, F. R. The unfolded protein response and cell fate control. *Mol. Cell*. <https://doi.org/10.1016/j.molcel.2017.06.017> (2018).
6. Urra, H., Dufey, E., Avril, T., Chevet, E. & Hetz, C. Endoplasmic reticulum stress and the hallmarks of Cancer. *Trends Cancer* **2**, 252–262 (2016).
7. Wang, M. & Kaufman, R. J. Protein misfolding in the endoplasmic reticulum as a conduit to human disease. *Nature* **529**, 326–335 (2016).
8. Hollien, J. & Weissman, J. S. Decay of endoplasmic reticulum-localized mRNAs during the unfolded protein response. *Science* **313**, 104–107 (2006).
9. Hollien, J. et al. Regulated Ire1-dependent decay of messenger RNAs in mammalian cells. *J. Cell Biol.* <https://doi.org/10.1083/jcb.200903014> (2009).
10. Maurel, M., Chevet, E., Tavernier, J. & Gerlo, S. Getting RIDD of RNA: IRE1 in cell fate regulation. *Trends Biochem. Sci.* **39**, 245–254 (2014).
11. Han, D. et al. IRE1 α kinase activation modes control alternate endoribonuclease outputs to determine divergent cell fates. *Cell* **138**, 562–575 (2009).
12. Acosta-Alvarez, D. et al. XBP1 controls diverse cell type- and condition-specific transcriptional regulatory networks. *Mol. Cell* **27**, 53–66 (2007).
13. Li, H., Korennykh, A. V., Behrman, S. L. & Walter, P. Mammalian endoplasmic reticulum stress sensor IRE1 signals by dynamic clustering. *Proc. Natl Acad. Sci. USA* **107**, 16113–16118 (2010).
14. Carreras-Sureda, A. et al. Non-canonical function of IRE1 α determines mitochondria-associated endoplasmic reticulum composition to control calcium transfer and bioenergetics. *Nat. Cell Biol.* **21**, 755–767 (2019).
15. Sepulveda, D. et al. Interactome screening identifies the ER luminal chaperone Hsp47 as a regulator of the unfolded protein response transducer IRE1 α . *Mol. Cell* **69**, 238–251.e8 (2018).
16. Cross, B. C. S. et al. The molecular basis for selective inhibition of unconventional mRNA splicing by an IRE1-binding small molecule. *Proc. Natl Acad. Sci. USA* **109**, E869–E878 (2012).
17. Burgess, R. C. & Misteli, T. Not all DDRs are created equal: non-canonical DNA damage responses. *Cell* **162**, 944–947 (2015).
18. Kitagawa, R., Bakkenist, C. J., McKinnon, P. J. & Kastan, M. B. Phosphorylation of SMC1 is a critical downstream event in the ATM-NBS1- BRCA1 pathway. *Genes Dev.* <https://doi.org/10.1101/gad.1200304> (2004).
19. White, D. et al. The ATM substrate KAP1 controls DNA repair in heterochromatin: Regulation by HP1 proteins and serine 473/824 phosphorylation. *Mol. Cancer Res.* <https://doi.org/10.1158/1541-7786.MCR-11-0134> (2012).
20. Hur, K. Y. et al. IRE1 α activation protects mice against acetaminophen-induced hepatotoxicity. *J. Exp. Med.* **209**, 307–318 (2012).
21. Oikawa, D., Tokuda, M., Hosoda, A. & Iwawaki, T. Identification of a consensus element recognized and cleaved by IRE1 α . *Nucleic Acids Res.* **38**, 6265–6273 (2010).
22. Chowdhury, D. et al. γ -H2AX dephosphorylation by protein phosphatase 2A facilitates DNA double-strand break repair. *Mol. Cell* **20**, 801–809 (2005).
23. Jha, S., Shibata, E. & Dutta, A. Human Rvb1/Tip49 is required for the histone acetyltransferase activity of Tip60/NuA4 and for the downregulation of phosphorylation on H2AX after DNA damage. *Mol. Cell Biol.* **28**, 2690–2700 (2008).
24. Hetz, C., Chevet, E. & Oakes, S. A. Proteostasis control by the unfolded protein response. *Nat. Cell Biol.* **17**, 829–838 (2015).
25. Urra, H. et al. IRE1 α governs cytoskeleton remodelling and cell migration through a direct interaction with filamin A. *Nat. Cell Biol.* **20**, 942–953 (2018).
26. Morita, S. et al. Targeting ABL-IRE1 α signaling spares ER-stressed pancreatic β cells to reverse autoimmune diabetes. *Cell Metab.* **25**, 883–897.e8 (2017).
27. Greuber, E. K., Smith-Pearson, P., Wang, J. & Pendergast, A. M. Role of ABL family kinases in cancer: from leukaemia to solid tumours. *Nat. Rev. Cancer* **13**, 559–571 (2013).
28. Coelho, D. S. et al. Xbp1-Independent Ire1 signaling is required for photoreceptor differentiation and rhabdomere morphogenesis in Drosophila. *Cell Rep.* **5**, 791–801 (2013).
29. Lee, A.-H., Scapa, E. F., Cohen, D. E. & Glimcher, L. H. Regulation of hepatic lipogenesis by the transcription factor XBP1. *Science*. <https://doi.org/10.1126/science.1158042> (2008).
30. Lee, J. H. et al. ATM directs DNA damage responses and proteostasis via genetically separable pathways. *Sci. Signal.* **11**, 1–18 (2018).
31. Edifizi, D. et al. Multilayered reprogramming in response to persistent DNA damage in *C. elegans*. *Cell Rep.* **20**, 2026–2043 (2017).
32. Gomes-da-Silva, L. C. et al. Photodynamic therapy with redaporfin targets the endoplasmic reticulum and Golgi apparatus. *EMBO J.* **37**, e98354 (2018).
33. Zheng, P. et al. DNA damage triggers tubular endoplasmic reticulum extension to promote apoptosis by facilitating ER-mitochondria signaling. *Cell Res.* **28**, 833–854 (2018).
34. Cabrera, E. et al. PERK inhibits DNA replication during the unfolded protein response via Claspin and Chk1. *Oncogene* **36**, 678–686 (2017).
35. Weatherbee, J. L. et al. ER stress in temozolomide-treated glioblastomas interferes with DNA repair and induces apoptosis. *Oncotarget* **7**, 43820–43834 (2016).
36. Oommen, D. & Prise, K. M. Down-regulation of PERK enhances resistance to ionizing radiation. *Biochem. Biophys. Res. Commun.* **441**, 31–35 (2013).
37. Yamamori, T., Meike, S., Nagane, M., Yasui, H. & Inanami, O. ER stress suppresses DNA double-strand break repair and sensitizes tumor cells to ionizing radiation by stimulating proteasomal degradation of Rad51. *FEBS Lett.* **587**, 3348–3353 (2013).
38. Bobrovnikova-Marjon, E. et al. PERK promotes cancer cell proliferation and tumor growth by limiting oxidative DNA damage. *Oncogene* **29**, 3881–3895 (2010).
39. Huang, C. et al. Identification of XBP1-u as a novel regulator of the MDM2/p53 axis using an shRNA library. *Sci. Adv.* <https://doi.org/10.1126/sciadv.1701383> (2017).
40. Lhomond, S. et al. Dual IRE1 RNase functions dictate glioblastoma development. *EMBO Mol. Med.* **10**, e7929 (2018).
41. Pluquet, O. et al. Posttranscriptional regulation of per1 underlies the oncogenic function of IRE α . *Cancer Res.* <https://doi.org/10.1158/0008-5472.CAN-12-3989> (2013).
42. Tavernier, S. J. et al. Regulated IRE1-dependent mRNA decay sets the threshold for dendritic cell survival. *Nat. Cell Biol.* **19**, 698–710 (2017).
43. Osorio, F. et al. The unfolded-protein-response sensor IRE-1 α regulates the function of CD8 α ⁺ dendritic cells. *Nat. Immunol.* **15**, 248–257 (2014).
44. Lerner, A. G. et al. IRE1 α induces thioredoxin-interacting protein to activate the NLRP3 inflammasome and promote programmed cell death under irremediable ER stress. *Cell Metab.* **16**, 250–264 (2012).
45. Greenman, C. et al. Patterns of somatic mutation in human cancer genomes. *Nature* **446**, 153–158 (2007).
46. Hetz, C. et al. Proapoptotic BAX and BAK modulate the unfolded protein response by a direct interaction with IRE1 α . *Science* **312**, 572–576 (2006).
47. Rodriguez, D. A. et al. BH3-only proteins are part of a regulatory network that control the sustained signalling of the unfolded protein response sensor IRE1 α . *EMBO J.* **31**, 2322–2335 (2012).
48. Lisbona, F. et al. BAX Inhibitor-1 is a negative regulator of the ER stress sensor IRE1 α . *Mol. Cell*. <https://doi.org/10.1016/j.molcel.2009.02.017> (2009).
49. Bravo-San Pedro, J. M., Kroemer, G. & Galluzzi, L. Autophagy and mitophagy in cardiovascular disease. *Circ. Res.* <https://doi.org/10.1161/CIRCRESAHA.117.311082> (2017).
50. Olive, P. L. & Ban ath, J. P. The comet assay: a method to measure DNA damage in individual cells. *Nat. Protoc.* **1**, 23–29 (2006).
51. Fenech, M. Cytokinesis-block micronucleus cytome assay in lymphocytes. *Nat. Protoc.* **2**, 1084–1104 (2007).
52. Mendez, A. S. et al. Endoplasmic reticulum stress-independent activation of unfolded protein response kinases by a small molecule ATP-mimic. *Elife* **4**, 1–27 (2015).
53. Iwawaki, T., Akai, R., Yamanaka, S. & Kohno, K. Function of IRE1 α in the placenta is essential for placental development and embryonic viability. *Proc. Natl Acad. Sci. USA* <https://doi.org/10.1073/pnas.0903775106> (2009).
54. Nakama, T. et al. Etoposide prevents apoptosis in mouse liver with D-Galactosamine/lipopolysaccharide-induced fulminant hepatic failure resulting in reduction of lethality. *Hepatology* **33**, 1441–1450 (2001).
55. Graf, U. et al. Somatic mutation and recombination test in Drosophila melanogaster. *Environ. Mutagen.* **6**, 153–188 (1984).
56. Castillo, K. et al. BAX inhibitor-1 regulates autophagy by controlling the IRE1 α branch of the unfolded protein response. *EMBO J.* **30**, 4465–4478 (2011).
57. Rojas-Rivera, D. et al. TMBIM3/GRINA is a novel unfolded protein response (UPR) target gene that controls apoptosis through the modulation of ER calcium homeostasis. *Cell Death Differ.* **19**, 1013–1026 (2012).
58. Cruz, C., Glavic, A., Casado, M. & De Celis, J. F. A gain-of-function screen identifying genes required for growth and pattern formation of the Drosophila melanogaster wing. *Genetics* **183**, 1005–1026 (2009).

Acknowledgements

We thank Dr. Takao Iwawaki for providing IRE1 flox mice. We thank Dr. David Ron for providing IRE1 null MEFs. We thank Dr. Alexis Rivas for assistance with Cellomics array scan (FONDEQUIP EQM120164). We thank Javiera Ponce for assistance with animal care. ANID/FONDAP program 15150012, Millennium Institute P09-015-F, CONICYT-Brazil 441921/2016-7, FONDEF ID16I10223, FONDEF D11E1007, and FONDECYT 1180186 (C.H.), and Ecos-Conicyt n $^{\circ}$ C17S02 (C.H.). In addition, we thank the support from the U.S. Air Force Office of Scientific Research FA9550-16-1-0384, and Muscular Dystrophy Association, US Office of Naval Research-Global (ONR-G) N62909-16-1-2003, and the European Commission R&D MSCA-RISE-734749 (INSPIRED). We thank the support from: FONDECYT 11180825 (H.U.); FONDECYT 3190738 (A.I.S.);

FONDECYT 3180427 (Y.H.), FONDECYT 3150113 (A.C.-S.), and EMBO ASTF 385-2016 (A.C.-S.); CONICYT fellowship (PCHA/Doctorado Nacional/2016-21160232) (M.G.-Q.), MSCA RISE-734749 (INSPIRED) (M.Q.-G.) and FONDAP-GERO-15150012 (A.I.S., P.P.). A.G. is supported by FONDAP-CRG-15090007 and ACT1401. DAA was supported by an Irvington Postdoctoral Fellowship of the Cancer Research Institute. A.A. is supported by FONDECYT 1161065 and AFB170005. G.K. is supported by the Ligue contre le Cancer (équipe labellisée); Agence National de la Recherche (ANR)—Projets blancs; ANR under the frame of E-Rare-2, the ERA-Net for Research on Rare Diseases; Association pour la recherche sur le cancer (ARC); Cancéropôle Ile-de-France; Chancellerie des universités de Paris (Legs Poix), Fondation pour la Recherche Médicale (FRM); a donation by Elior; the European Commission (ArtForce); European Research Area Network on Cardiovascular Diseases (ERA-CVD, MINOTAUR); the European Research Council (ERC); Fondation Carrefour; Institut National du Cancer (INCa); Inserm (HTE); Institut Universitaire de France; LeDucq Foundation; the LabEx Immuno-Oncology; the RHU Torino Lumière; the Seerave Foundation; the SIRIC Stratified Oncology Cell DNA Repair and Tumor Immune Elimination (SOCRATE); the SIRIC Cancer Research and Personalized Medicine (CARPEM); and the Paris Alliance of Cancer Research Institutes (PACRI). P.M.D was supported by FCT LISBOA-01-0145-FEDER-007660, PTDC/NEU-NMC/2459/2014 and IF/00697/2014 (Portugal). R.P. is supported by Fondation pour la Recherche Médicale (FMR, DEQ20180339169) and Institut National de la Santé et de la Recherche Médicale (INSERM). E.C. is supported by Institut National du Cancer (INCa PLBIO), ANR under the frame of ERANET (ERAAT) and EU H2020 MSCA ITN-675448 (TRAINERS) and MSCA RISE-734749 (INSPIRED).

Author contributions

E.D., M.G.-Q., and A.I.S.: conceived and designed the project, carried out experimental work with cell culture and mouse models, and wrote the paper; J.M.B., C.E., H.U., D.S., P.P., A.C.-S., Y.H., E.A.S., D.G., C.V., A.P., D.A.-A., G.C., P.G., A.G.: carried out experimental work and interpreted data; P.G. and E.A.S.: performed bioinformatics work, interpreted data and wrote the manuscript; A.A., P.M.D., Contributed to project design and data interpretation; C.H., P.W., G.K., R.P., E.C.: contributed to project design, interpreted data and wrote the paper.

Competing interests

The authors declare no competing interests.

Additional information

Supplementary information is available for this paper at <https://doi.org/10.1038/s41467-020-15694-y>.

Correspondence and requests for materials should be addressed to C.H.

Peer review information *Nature Communications* thanks Martin Lavin, Hermann Steller and the other, anonymous, reviewer(s) for their contribution to the peer review of this work. Peer reviewer reports are available.

Reprints and permission information is available at <http://www.nature.com/reprints>

Publisher's note Springer Nature remains neutral with regard to jurisdictional claims in published maps and institutional affiliations.



Open Access This article is licensed under a Creative Commons Attribution 4.0 International License, which permits use, sharing, adaptation, distribution and reproduction in any medium or format, as long as you give appropriate credit to the original author(s) and the source, provide a link to the Creative Commons license, and indicate if changes were made. The images or other third party material in this article are included in the article's Creative Commons license, unless indicated otherwise in a credit line to the material. If material is not included in the article's Creative Commons license and your intended use is not permitted by statutory regulation or exceeds the permitted use, you will need to obtain permission directly from the copyright holder. To view a copy of this license, visit <http://creativecommons.org/licenses/by/4.0/>.

© The Author(s) 2020